WILEY-VCH

LASER
&PHOTONICS
REVIEWS

Research Article | Full Access

# A Versatile Photochromic Dosimeter Enabling Detection of X-Ray, Ultraviolet, and Visible Photons

Zetian Yang, Jieqi Hu, David Van der Heggen, ✉, Mengmeng Jiao, Ang Feng, Henk Vrielinck, ✉, Philippe F. Smet, Dirk Poelman ✉

First published: 29 January 2023 | https://doi.org/10.1002/lpor.202200809

# A Versatile Photochromic Dosimeter enabling Detection of X-ray, Ultraviolet, and Visible Photons

*Zetian Yang, Jieqi Hu, David Van der Heggen*, Mengmeng Jiao, Ang Feng, Henk Vrielinck*, Philippe F. Smet and Dirk Poelman**

Z. Yang, J. Hu, Dr. D. Van der Heggen, Dr. M. Jiao, Dr. A. Feng, Prof. P. F. Smet, Prof. D. Poelman
LumiLab, Department of Solid State Sciences, Ghent University, Krijgslaan 281-S1, Ghent B-9000, Belgium
E-mail: David.VanderHeggen@ugent.be; Dirk.Poelman@ugent.be

Prof. H. Vrielinck
Electron Magnetic Resonance Group, Department of Solid State Sciences, Ghent University, Krijgslaan 281-S1, B-9000, Ghent, Belgium
E-mail: Henk.Vrielinck@ugent.be

Keywords: passive dosimeter, $BaMgSiO_4$, photochromic materials, cumulative dose, coloring and bleaching, oxygen vacancies

An accurate measurement of radiation doses is required to ensure efficient use of electromagnetic radiation in medical diagnostics, agriculture or general lighting applications. Yet, existing dosimeters usually face the issues of cumbersome manipulation, time-consuming analysis or power-supply requirement. Here, an all-round dosimeter is reported based on $BaMgSiO_4$, a photochromic material that exhibits a reversible white-pink color change upon irradiation. Electron paramagnetic resonance measurements under *in situ* coloring and bleaching reveal that the charge carrier trapping and de-trapping at oxygen vacancy-related defects determine the photochromic behavior. This can be utilized for dosimetry of X-rays, ultraviolet and visible light, as the coloring and bleaching are dependent on the irradiation wavelength and the dose. The distinct color variation of $BaMgSiO_4$ allows for on-site measurement of irradiation doses by a colorimetric method, and the special wavelength-responsive behavior in the ultraviolet region is suitable for personal solar ultraviolet light monitoring. By virtue of good stability and excellent cycling robustness, $BaMgSiO_4$ can be an ideal integrating detector for X-rays, ultraviolet and visible light dosimetry. A prototype device

is also developed for long-duration daylight measurements. These findings enhance the understanding of the photochromic behavior in inorganic materials and can stimulate the exploration of new photochromic dosimeters.

## 1. Introduction

Electromagnetic radiation in the X-ray, ultraviolet (UV) and visible range is extensively utilized in various fields including medical diagnostics, food processing, photodynamic therapy, sterilization and indoor plant lighting.[1-3] Appropriate electromagnetic radiation can offer certain benefits, for example, killing malignant tumors using X-ray irradiation, stimulating vitamin D production upon UV exposure and regulating plant growth through tuning the quantity and directionality of UV-visible light.[4-6] However, a series of risks such as skin cancer, photoaging, sleep and mood disorders, reduction in crop yields and damage of dyed artworks can also be induced by excessive exposure.[7-9] These risks are wavelength-specific and can depend on the cumulative dose. To avoid the adverse influence of both under- and over-exposure, light dosimeters enabling an accurate measurement of the cumulative dose of different types of electromagnetic radiation are required. Light dosimeters can be classified into two different types: active dosimeters and passive dosimeters.[10, 11] Examples of active dosimeters are ionization chambers, scintillation detectors and semiconductor detectors, which convert light into electrical charges and can measure an instantaneous dose rate or light intensity.[12-25] However, this type of detector usually requires a power supply and a real-time data processing for long-duration measurements, making them bulky and costly to provide integrated dose information.[26] In contrast, passive dosimeters can store the radiation dose information during the measurement. They are subsequently read out by optical, electrical or thermal stimuli and provide a cumulative dose information, which has multiple advantages such as cost-effectiveness, compact size and robust structure and can achieve power-free operation.[27-30]

The well-developed passive dosimeters mainly include luminescent materials and photochromic materials.[11, 17, 29, 31-37] Luminescent materials operating on the principles of thermoluminescence (LiF:Mg,Ti and $CaF_2$:Dy), optically stimulated luminescence ($Al_2O_3$:C and BeO, e.g.) and radio-photoluminescence (Ag-doped phosphate glass and $Al_2O_3$:C,Mg, e.g.), whose luminescence intensity scales with the dose absorbed from the radiation field, are widely used for ionizing radiation measurements.[29, 32, 38] However, such dosimeters usually lack UV-visible light response and require specific readout instruments and complex calibration for practical dosimetry. Photochromic materials exhibit a transformation between two states with

different absorption spectra upon irradiation, which allows for direct readout and on-site assessment of the radiation dose.[37, 39-44] Also, both qualitative and quantitative radiation dose measurement can be accomplished by a colorimetric method and by measuring the absorption spectra, respectively. In combination with convenient operation and simple configuration, photochromic dosimeters are regarded as promising dosimeters for continuous light sensing applications.[30, 33, 45-49] Different types of photochromic dosimeters such as metal-organic complexes (uranyl-organic framework), photodegradable dyes (polysulfone and polyphenylene oxide, e.g.), minerals ($Na_8Al_6Si_6O_{24}(Cl,S)_2$), hydrogel (methacrylic acid, gelatine and tetrakis, e.g.) and transition metal oxides ($TiO_2$) have been developed, yet most of these dosimeters are non-reusable, require a long analysis time, have a poor stability or show a weak color contrast.[28, 34-37, 45, 46, 50-63] For instance, the colored transition metal oxides usually spontaneously recover to their initial state over several hours under ambient air conditions while hydrogels require a long post-irradiation waiting time (typically > 24 hours) for the polymerization process, and coordination polymers are restricted to single-use operation.[30, 46, 52, 61, 64, 65] Moreover, it is desirable for specific applications that the dosimeter can not only measure the dose of a monochromatic light source but also exhibits a specific wavelength-responsive behavior in a certain spectral band. For example, dosimeters for personal solar UV monitoring need to have a spectral response adapted to the UV sensitivity of human skin while photodynamic therapy requires a similar wavelength response between dosimeter and lesion, which is still challenging for current dosimeters.[33, 66] As a result, the development of light dosimeters that combine a convenient operation, special wavelength-responsive behavior, reusability and cost-effectiveness remains ongoing.

Herein we demonstrate an integrating dosimeter for X-rays, UV as well as visible light, based on $BaMgSiO_4$ (see **Figure 1**), a photochromic material that exhibits a reversible white to pink color change upon irradiation.[67-69] *In situ* electron paramagnetic resonance (EPR) experiments reveal that charge carriers trapping and de-trapping at oxygen vacancies determine the photochromic behavior. The photochromic effect can be significantly enhanced by manipulating the defect concentration. Irradiation wavelength- and power density-dependent coloring and bleaching processes are also systematically investigated to explore the potential use of $BaMgSiO_4$ as an integrating radiation dosimeter. It is shown that the photochromic transition from white to pink enables X-rays and UV light dosimetry while the reverse pink to white bleaching process can be used for visible light dosimetry. Also, the colored state has good stability and the photochromic behavior exhibits excellent cycling robustness, which ensures the dosimeter can be re-used. On-site qualitative assessment of radiation doses is accomplished

in $BaMgSiO_4$ by a colorimetric method and quantitative dose information can be obtained by measuring the reflection spectrum or using the red to green pixel intensity on a photograph under standard lighting conditions. Moreover, the special wavelength-responsive behavior of $BaMgSiO_4$ in the UV band is attractive for personal solar UV monitoring. These results show the great potential of $BaMgSiO_4$ for X-ray, UV and visible radiation dosimetry and are expected to stimulate research on new photochromic dosimeters.

## 2. Results and Discussion

### 2.1. $BaMgSiO_4$ synthesized in different conditions and their photochromic behavior

The XRD patterns of powder $BaMgSiO_4$ are well indexed by the reference card of ICSD 81-2317 (see **Figure 2**a), indicating that a pure hexagonal phase with a space group of $P6_3$ is formed in all samples, irrespective of the synthesis atmosphere. $BaMgSiO_4$ belongs to the stuffed tridymite structure, as displayed in Figure 2b.[70] Tetrahedrons of $[SiO_4]^{4-}$ and $[MgO_4]^{4-}$ are linked by corner-sharing to build up the tridymite skeleton and the tunnels are stuffed with $Ba^{2+}$ ions. The photochromic behavior of $BaMgSiO_4$ sintered under different conditions is presented in Figure 2c. Before irradiation, all samples exhibit a high reflectivity in the visible region. After 250 nm irradiation, a decline of reflectivity is observed in all samples. The reflectivity change of the sample sintered in $N_2$+$H_2$ conditions is most pronounced (see Figure 2d) and the reflectivity difference is boosted about four times in comparison with that of the sample sintered in air. Also, two new absorption peaks centered at 308 nm and 392 nm emerge in $BaMgSiO_4$ sintered in $N_2$+$H_2$, in addition to the common absorption peaks at 523 nm and 685 nm (see Figure 2d). Meanwhile, a significant color change from white to pink is observed in $BaMgSiO_4$ sintered in $N_2$+$H_2$ during the photochromic process, while the samples prepared in air or $N_2$ only show a relatively weak color change (see Figure 2e), which is in line with the reflectivity change during the photochromic processes.

### 2.2. *In situ* EPR measurements and the mechanism of photochromism

EPR measurements were carried out to study the charge transfer processes related to the photochromic transition in $BaMgSiO_4$ (see **Figure 3**). In Figure 3a, the EPR spectra of the samples in non-colored state are shown. Multiple single-line EPR signals are observed: at g = 2.0034, most prominent in the sample prepared in air or $N_2$, at g = 1.9795, seen in all samples but more abundant in the sample prepared in $N_2$ or $N_2$+$H_2$, and at g = 1.9741, only clearly observable in the sample prepared in $N_2$+$H_2$. In the spectra of all samples also a complicated broad spectral component occurs, which can be attributed to Mn-trace impurities in the sample, based on a comparison with the EPR spectrum of intentionally Mn-doped $BaMgSiO_4$ (see Figure S1a, Supporting Information). EPR is known to be quite sensitive to $Mn^{2+}$, which was

also found back as trace impurity in the $SiO_2$ precursor (see Figure S1b, Supporting Information). The signal at g =2.0034 is very similar in g-value and line width to an EPR component observed in intentionally Fe-doped $BaMgSiO_4$ (see Figure S1c, Supporting Information). For samples sintered in air or $N_2$, Fe ions mainly exist in the paramagnetic state ($Fe^{3+}$), resulting in a stronger EPR signal. The origin of the signal at g = 1.9795 is not entirely clear, which might originate from another type of impurity ion introduced from the precursor materials, but at this point it is not possible to assign this signal to a specific defect. Finally, a strong EPR peak at 1230 mT (g = 1.9741) is observed in $BaMgSiO_4$ sintered in $N_2$+$H_2$, is also present with much lower intensity in $BaMgSiO_4$ sintered in $N_2$ and remains undetected in $BaMgSiO_4$ sintered in air, which can be ascribed to an electron trapped at an oxygen vacancy, *i.e.* $V_O^{\cdot}$ or $F^+$.[71-73] It is, indeed, reasonable that a reducing atmosphere is favorable for the formation of $V_O^{\cdot}$, for which a g-factor with a negative shift from the free-electron value is expected. This center has been reported before in $BaMgSiO_4$ synthesized in reducing atmosphere.[71, 72]

In previous research, the photochromic behavior of certain inorganic oxide materials was often linked to the formation of defects related to oxygen vacancies based on the EPR results.[67, 68, 74] However, most studies, using *ex situ* illumination to induce the photochromic effect, failed to provide experimental evidence that actually links the EPR signals to the observed photochromic effect, as the EPR signal intensity can strongly depend on the sample position in the cavity. Furthermore, intensity changes during photochromic coloring and bleaching often turn out to be limited. To improve this approach, changes in the EPR signals upon coloring and bleaching should be observed *in situ*. The following experiments were performed for both *in situ* bleaching and coloring, starting from a colored or bleached sample, respectively. For the bleaching process, the sample was first colored *ex situ* under 302 nm (see Figure 3c) or *in situ* using 365 nm (see Figure 3d) irradiation and then *in situ* bleached under 450 nm or 490 nm irradiation. For the coloring process, the sample was first *ex situ* bleached under 490 nm irradiation and then *in situ* colored under 365 nm irradiation (see Figure 3e). It should be mentioned that it only makes sense to analyze the relative intensity change among these different experiments rather than the absolute intensity change. The latter is inevitably influenced substantially by the sample quantity and position in the EPR cavity in the different measurements. As shown in Figure 3c-3e, the EPR signal (g = 1.9741) related to $V_O^{\cdot}$ increases for the bleaching process while it decreases for the coloring process (see Figure 3f for the EPR signal differences). It is also seen that the relative signal intensity change obtained in the sample first colored under 302 nm irradiation (see Figure 3c) is larger than that first colored under 365

nm irradiation (see Figure 3d). This is consistent with the wavelength-dependent coloring behavior (see Figure 3b), in which 302 nm exhibits a more effective coloring effect in comparison with 365 nm. In the coloring process under 302 nm irradiation, more defects are involved and hence the relative EPR signal intensity change is larger. At intermediate steps in the coloring and bleaching, correlated gradual changes in the EPR spectrum intensities are seen (see Figure S1d-S1f). Apart from the EPR signal (g = 1.9741) related to $V_O^{\cdot}$, the EPR signal at g = 1.9795 also shows intensity changes but only when colored under 302 nm irradiation (see Figure 3c), while no such change was detected when colored under 365 nm irradiation (see Figure 3d and 3e). This signal intensity change can be distinctly observed from the EPR signal difference (see Figure 3f). This phenomenon might be caused by the irradiation-induced redox processes of the involved defects, in which the energy of 302 nm radiation is sufficient to stimulate the reduction or oxidation process. Such a phenomenon is also seen in certain radio-photoluminescent materials.[75]

Based on the above results, we can safely state that the trapping and de-trapping of an electron at $V_O^{\cdot}$ are indeed responsible for the photochromic behavior in $BaMgSiO_4$. The strongly enhanced photochromic effect obtained in $BaMgSiO_4$ sintered in $N_2$+$H_2$ is ascribed to the formation of additional oxygen vacancies. During the coloring process some $F^+$ centers capture one more electron to form F centers, leading to the decrease of the corresponding EPR signal at g = 1.9741. Inversely, during the bleaching process, the F centers release the trapped electron and revert to $F^+$ centers, resulting in the increase of the EPR signal at g = 1.9741. In the following parts, we mainly focus on $BaMgSiO_4$ sintered in $N_2$+$H_2$ condition and explore its potential for dosimetry applications because of its superior photochromic behavior.

**2.3. Irradiation wavelength- and power-dependent photochromic behavior**

To assess the maximum coloring or bleaching that can be achieved when using different wavelengths, a sufficiently long irradiation was performed at each wavelength with a NT340 series tunable laser to ensure the sample reached the maximally bleached or colored saturation state. As shown in **Figure 4**a, the sample starts to be colored when the irradiation wavelength is less than 475 nm, and the coloring effect gradually strengthens as the irradiation wavelength decreases. In addition, two new absorption peaks (centered at 308 nm and 392 nm) appear when the sample was irradiated with shorter wavelengths (< 400 nm) in comparison with the absorption upon irradiation at longer wavelengths (see Figure S2, Supporting Information), suggesting that the defects related to the absorption bands at shorter wavelengths can only be activated upon high-energy photon irradiation. It should be mentioned that the absorption bands at higher energy display a different dose dependency (see Figure S3, Supporting Information).

Only the absorption band centered at 523 nm is induced in the initial stage of irradiation even under irradiation with high-energy photons followed by the appearance of the absorption peaks at shorter wavelengths upon further irradiation. In this sense, it is assumed that these two new absorption peaks are linked to another type of defects with different trap depths. Next to UV, it was found that $BaMgSiO_4$ could also be colored using X-rays (see Figure S4, Supporting Information). The similar photochromic behavior under X-rays and UV indicates that the same defects are involved in both irradiation methods.

In a next step, the wavelength dependency of the bleaching of previously fully colored samples was investigated. Bleaching occurred when the irradiation wavelength was longer than 350 nm (see Figure 4b), and the absorption bands in the visible region could be almost completely bleached upon irradiation at long wavelengths (≥ 525 nm). The remaining weak absorption at 523 nm was difficult to be bleached because the sample exhibited only weak absorption of the irradiation light at this state. Although the shorter wavelengths of 425 nm and 475 nm were not effective to bleach the absorption centered at 523 nm, they exhibited a better bleaching effect for the absorption bands at higher energy (308 nm and 392 nm) in comparison to bleaching with longer wavelengths. This means that the de-trapping of the electrons related to the absorption centered at 308 nm and 392 nm also requires relative high-energy photon stimulation. This is consistent with the results of thermal bleaching experiments (see Figure S5, Supporting Information), in which the absorption bands at shorter wavelengths can only be completely bleached at higher temperatures. It should be mentioned that the absorption band at 523 nm can already be completely bleached upon heating the sample at 285 °C (see Figure S5, Supporting Information). As a result, the absorption peak at 523 nm (from 470 nm to 570 nm) was used to evaluate the irradiation wavelength- and power-dependent photochromic behavior. Also, except for the bleached state in Figure 4a and Figure 4b, which refers to thermal treatment at 500 °C, other thermal bleached states refer to thermal treatment at 285 °C. The value of $\Delta R_1$ was used to evaluate the maximum coloring effect of each wavelength, which is defined as the integration of the reflectivity difference spectrum (bleached state minus after coloring state) from 470 nm to 570 nm. Similarly, the value of $\Delta r_1$, which integrates the reflectivity difference spectrum (after bleaching state minus colored state) within the range of 470 nm and 570 nm, was adopted to evaluate the maximum bleaching effect of each wavelength. The normalized maximum coloring and bleaching effect of different wavelengths is presented in Figure 4c. The two curves exhibit an apparent overlap in the range from 350 nm to 475 nm. This means that two processes, namely trapping and de-trapping, coexist when the sample is irradiated with light in this range, and a dynamic equilibrium between the two competing processes will be

reached upon long-time irradiation. This explains why the sample cannot be completely colored or bleached when the sample is irradiated with light in this range of 350 nm to 475 nm. Such a competition is also observed in certain other photochromic materials and persistent phosphors.[76, 77]

To obtain information on the wavelength dependency of the responsive behavior, the sample was first fully colored or bleached (250 nm irradiation using NT340 series tunable laser and 285 °C thermal treatment, respectively) and then irradiated using different wavelengths with the same power density and the same irradiation time, while remaining well below the saturation limit (see Figure S6, Supporting Information). It was shown that the sample could be colored upon irradiation at different wavelengths in the range of 302 nm to 430 nm while some wavelengths showed a more efficient coloring effect (see Figure S6a, Supporting Information). Similar behavior was also observed for the bleaching process (see Figure S6b, Supporting Information). The normalized wavelength-responsive behaviors for the coloring and bleaching processes are presented in Figure 4d, in which the value of $\Delta R_1$ and $\Delta r_1$ are also adopted to evaluate the coloring and bleaching effectiveness, respectively. The wavelength-responsive behavior for the coloring processes matches the absorption spectrum of the sample in the bleached state, while the wavelength-responsive behavior for the bleaching processes is consistent with the absorption characteristic of the sample in the colored state except for a slight deviation at short wavelengths (see Figure 4d). Here, the absorption spectrum ($F$(R)) was obtained from the diffuse reflectance spectra based on the Kubelka-Munk model.[78] These results indicate that the effectiveness of different wavelengths for coloring or bleaching is mainly determined by the absorption properties of the defects involved. A high absorption means that more photons of incident light can participate in the coloring or bleaching processes. Also, the special wavelength-responsive behavior of $BaMgSiO_4$ in the UV region makes it attractive for personal solar ultraviolet light monitoring.

**2.4. Dosimetry properties of $BaMgSiO_4$ for X-rays, UV and visible light**

In the following, the operating principle and the response behavior of $BaMgSiO_4$ to different radiation types, integrated dose and dose rates are discussed. According to the wavelength-dependent coloring and beaching behavior, the coloring process can be used for X-rays and UV light dosimetry and the reverse bleaching process can be adopted for visible light dosimetry. For X-rays or UV light dosimetry the sample needs to be fully bleached first, while the sample needs to be fully colored for visible light dosimetry. Examples of reflectivity change under different amounts of X-rays, 365 nm UV and 620 nm light irradiation are presented in **Figure 5**a, 5d and 5g, respectively. The results show that the reflectivity gradually decreases upon X-

rays or 365 nm light irradiation and increases upon 620 nm light irradiation. Here, $\Delta R_1$ and $\Delta r_1$ are adopted as the dose response parameter of X-rays/365 nm and 620 nm light, respectively (see Figure 5b, 5e and 5h). The response parameter is linearly dependent on the integrated dose at the initial exposure stage and gradually reaches saturation under high integrated dose regardless of the irradiation source. For example, the dosimeter exhibits a linear response in the range of 1 Gy - 9 Gy under X-ray exposure (see Figure S7, Supporting Information), which is an ideal range for fractionated clinical radiotherapy dosimetry.[53, 64] The upper limit of dosimetry under X-rays, 365 nm and 620 nm irradiation is 165 Gy, 135 mJ $cm^{-2}$ and 224 J $cm^{-2}$, respectively. It should be mentioned that the sample can be further colored or bleached upon longer exposure, but the change in reflectance is less pronounced which is not of interest for dosimetry applications. The upper detection limit for 365 nm UV dosimetry is relatively small for continuous measurements but this value can be easily extended to higher integrated doses using a neutral density filter provided that the response of the dosimeter is independent of the irradiation intensity. In other words, the induced reflectivity change under a short time irradiation of photons with a high intensity should be the same as the result under a long time irradiation of photons with a low intensity. This was tested by changing the dose rate of the X-ray source and the power density of the LEDs (see Figure S8, Supporting Information). It is clear from Figure 5c, 5f and 5i that the response is indeed independent of the irradiation intensity. These results indicate that $BaMgSiO_4$ can be a promising dosimeter for continuous measurement of X-rays, UV or visible light.

**2.5. Practical application of the dosimeter for outside integrated daylight measurements**

The stability of the photochromic behavior was tested by measuring the reflectivity of the colored sample after different waiting durations (see Figure S9, Supporting Information). It was found that the signal fading is less than 8 % in 36 h (see **Figure 6**a), confirming an excellent stability at room temperature. The stable trapped state enables to use $BaMgSiO_4$ for long-time continuous measurements. For practical applications, it is also desirable that the dosimeter can be reused. Here, the cycling robustness of $BaMgSiO_4$ was evaluated by measuring the reflectivity upon alternating 250 nm irradiation and 285 $^oC$ thermal treatment (see Figure S10, Supporting Information) and the reflectivity at 523 nm is plotted as a function of cycling numbers. It is evident from Figure 6b that the photochromic behavior in $BaMgSiO_4$ possesses excellent cycling robustness, which confirms that the dosimeter can be used for accurate and reusable dose measurements.

Although a dosimetric measurement can be performed by detecting the reflectivity, a dedicated spectrophotometer is usually required for the readout process, which is not

convenient for practical applications. However, the reflectivity change indicates a distinct white to pink color change in $BaMgSiO_4$. This behavior makes it possible to quantify the integrated dose via a colorimetric method, removing the need for special instruments. To confirm this, the color of the sample after different doses of 365 nm irradiation was recorded with a digital camera under an incandescent lamp to prepare a color matching chart (see Figure 6c), in which the color and the integrated dose are in one-to-one correspondence. As a result, the color can be adopted as a reference for unknown doses. A prototype device was fabricated to demonstrate the dosimetry process, which consists of a sample and colorimetric cards (see Figure 6d). Using this device, the dose received can be conveniently read out by comparing with the colorimetric cards, which allows for on-site qualitative assessment of radiation doses. In combination with the features of ease of handling, low cost and special wavelength-responsive behavior, this device is suited as personal UV dosimeter.

Typically, only semi-quantitative dose information can be obtained by a colorimetric method. For more accurate dosimetry, the RGB components (red, green and blue) of the sample after different doses of irradiation were extracted. In comparison to $I_B/I_G$ or $I_R/I_B$, the white to pink color change in $BaMgSiO_4$ results in a larger variation of $I_R/I_G$ which was thus adopted as the response parameter as it allows to obtain a higher sensitivity. Photographs were taken under an incandescent lamp with a digital camera and the light source remained the same for different shots. Based on the photographs in Figure S11, Supporting Information, the relationship of $I_R/I_G$ as a function of 365 nm irradiation dose was established in Figure 6e. The increase of $I_R/I_G$ is sharp up to about 25 mJ $cm^{-2}$, where the sensitivity is very high. For higher doses, $I_R/I_G$ slowly grows until a saturation state is reached, which is similar to the behavior of the irradiation dose-dependent reflectivity change (see Figure 5e). The irradiation dose-dependent $I_R/I_G$ for the bleaching process was also established (see Figure 6f) based on the photographs in Figure S12, Supporting Information, in which $I_R/I_G$ gradually decreases with the increase of integrated dose. The reliability of this method was also tested by recoding $I_R/I_G$ upon alternating 365 nm irradiation and thermal bleaching for 10 cycles (see Figure S13, Supporting Information). It is shown that $I_R/I_G$ remains stable for both the colored and bleached state during cycling with a uncertainty less than 1%, indicating that this method can provide a good accuracy for dose measurement.

Compared to dosimeters previously reported, the $BaMgSiO_4$-based dosimeter possesses numerous advantages such as excellent stability, great cycling robustness, distinct color variation, large reflectivity change, broad spectral response and battery-free operation and can support on-site assessment of irradiation doses by a colorimetric method.[30, 45, 46, 53, 57, 58]

Particularly, according to the best of our knowledge, this is the first time that the irradiation wavelength- and power density-dependent coloring and bleaching processes are systematically investigated in photochromic dosimeters. This allows for more targeted dosimetry of specific wavelengths or certain bands. To demonstrate this, a proof of concept dosimeter was developed for continuous outside daylight measurement, which consists of a $BaMgSiO_4$ sample, a bandpass filter (centered at 368 nm, FWHM = 10 nm) and a neutral density filter (optical density: 0.52 at 368 nm). The bandpass filter ensured that the sample was exposed to nearly monochromatic light, and the neutral density filter was adopted to extend the dynamic dosimetry range thanks to the dose rate-independent response behavior (see Figure 5f). The sample was fully bleached by thermal treatment before dosimetry. During the measurement, an electronic lux-meter (TSL 2561, with a sensitivity extending to the near-UV) covered by the same bandpass filter was also put next to the sample to detect the real-time light intensity. The electronic lux-meter was also used to measure the intensity of the 365 nm LED, used in Figure 5e with the same power density, to establish the response curve. After exposure, the response parameter $\Delta R_1$ was measured and then compared with the response curve to read out the dose information. The real-time light intensity (red curve) shows a large variation during the measurement period as a result of weather changes (see Figure 6g). The average light intensity measured by the electronic lux-meter and the sample is presented in Figure 6g by the red bar and yellow bar, respectively. A good agreement is realized for the dose information obtained by two different methods with a slight deviation of ~5%, showing the potential of $BaMgSiO_4$-based light dosimeter for long-duration daylight sensing applications.

## 3. Conclusion

In this work, we demonstrate an integrating dosimeter for X-ray/UV/visible light based on the photochromic material $BaMgSiO_4$ which exhibits a reversible color change from white to pink upon irradiation. *In situ* EPR experiments reveal that the photochromic behavior is likely related to the electron trapping and de-trapping by singly-ionized oxygen vacancies-related defects. The photochromic effect can be significantly enhanced by optimizing the synthesis conditions to introduce more oxygen vacancies. The influence of the irradiation wavelength and the power density on the coloring and bleaching processes were systematically investigated. It was shown that the coloring process can be induced by X-rays or UV, while the bleaching process can be achieved upon visible light irradiation. Two competing processes of trapping and de-trapping occur when irradiating with a specific range of wavelengths. The effectiveness of different wavelengths for the coloring or bleaching processes is determined by the absorption properties of the host material and of the trapped electrons. In addition, the potential of $BaMgSiO_4$ for

dosimetry was evaluated. Good stability and excellent cycling robustness were obtained in $BaMgSiO_4$ together with a dose rate-independent response behavior. Furthermore, the apparent color change of $BaMgSiO_4$ during photochromic processes enables on-site convenient assessment of irradiation doses by direct visual inspection. Quantitative dose information can be obtained using the red to green pixel intensity or monitoring the UV-visible reflectance spectra. Finally, a prototype dosimeter was developed for continuous outside daylight measurements. In combination with the advantages of power-free, convenient readout processes, low cost and excellent stability, $BaMgSiO_4$ can be an ideal integrating dosimeter for versatile detection of X-rays, UV, and visible photons.

## 4. Experimental Section

*Sample Preparation*: $BaMgSiO_4$ was synthesized using a conventional solid-state reaction. $BaCO_3$ (Alfa Aesar, 99.8%), $4MgCO_3{\cdot}Mg(OH)_2{\cdot}5H_2O$ (Alfa Aesar, 98%) and $SiO_2$ (Alfa Aesar, 99.5%) were used as raw materials without further purification. 10 mol% of $H_3BO_3$ was added as the sintering aid. The raw materials were mixed stoichiometrically followed by ball milling with ethanol for 5 h at a rotating speed of 300 rpm. After drying in an oven at 60 $^oC$, the powders were mixed with 5 wt% polyvinyl alcohol and pressed into pellets with a diameter of 13 mm and a thickness of ~1.2 mm. The pellets of $BaMgSiO_4$ were sintered at 1200 °C under different conditions (air, $N_2$ and 90% $N_2$+10% $H_2$, labelled as $N_2$+$H_2$) for 5 h to obtain dense ceramics. For X-ray diffraction (XRD) measurement, the ceramic was ground to powder.

*Characterization:* Powder XRD patterns were collected using a Siemens D5000 diffractometer with Cu Kα1 radiation. The reflectance spectra were measured using a PerkinElmer Lambda 1050 UV-vis-NIR spectrophotometer equipped with a Spectralon-coated integrating sphere with PMT (photomultiplier) and InGaAs detectors. The wavelength-dependent maximum coloring and bleaching processes were carried out with a NT340 series tunable laser (EKSPLA, Lithuania). The wavelength-responsive behavior was measured using light-emitting diodes (LEDs) centered at 360 nm (FWHM = 14 nm), 370 nm (FWHM = 11 nm), 380 nm (FWHM = 12 nm), 390 nm (FWHM = 14 nm), 400 nm (FWHM = 15 nm), 410 nm (FWHM = 21 nm), 430 nm (FWHM = 20 nm), 450 nm (FWHM = 19 nm), 470 nm (FWHM = 22 nm), 490 nm (FWHM = 29 nm), 525 nm (FWHM = 35 nm), 545 nm (FWHM = 40 nm), 590 nm (FWHM = 14 nm), 605 nm (FWHM = 15 nm), 645 nm (FWHM = 17 nm), 670 nm (FWHM = 24 nm), 710 nm (FWHM = 22 nm) and 770 nm (FWHM = 25 nm). A UV lamp (Germicidal Hg lamp) centered at 302 nm (FWHM = 38 nm) was also used for the coloring experiment. For those experiments, the current was adjusted to arrive at a power density (at the sample surface) of 1.3 mW $cm^{-2}$ and 3.0 mW $cm^{-2}$ for the wavelength-dependent effective coloring and bleaching process,

respectively. The power density of LEDs and the UV lamp was measured using an S401C thermal power sensor coupled to a PM100 readout unit (Thorlabs). The time-resolved daylight intensity was measured using an electronic TSL 2561 lux meter (Adafruit). The thermal bleaching experiments at 285 °C were performed on a hot plate in air for 5 minutes and the thermal treatment at 500 $^{o}$C was carried out in a muffle furnace for 5 minutes. Electron paramagnetic resonance (EPR) measurements were performed at room temperature on a Bruker ElexSys E500 spectrometer operating at Q-band (34 GHz) and with 1 - 5 mW microwave power. A Pendulum CNT-90XL frequency counter was used to measure the microwave frequency and a Bruker NMR ER 035M Gaussmeter for the magnetic field. *In situ* EPR measurements were performed using an optical fiber to transmit light into the sample holder to *in situ* color or bleach the sample. A plastic optical fiber and a quartz fiber were used to guide visible light and UV light, respectively. Photographs were taken with a Nikon D3200 camera (Nikon Corporation; Japan) in raw format. The photographs for extracting RGB (red, green and blue) values purpose were taken with a fixed exposure time of 1/80 s and ISO of 6400. The RGB values of the photograph were extracted using MATLAB. A Siemens D5000 X-ray diffractometer (Cu anode, not filtered) was used as the X-ray irradiation source. Air-kerma rates of 5.625 Gy min$^{-1}$ and 1.875 Gy min$^{-1}$ were generated at the position of the sample when the X-ray diffractometer operated at 40 kV, 15 mA, and 40 kV, 5 mA, respectively. LEDs centered at 365 nm (FWHM = 16 nm) and 620 nm (FWHM = 20 nm) were used as the UV and visible light irradiation source to establish the dose-response behavior, respectively.

## Supporting Information

Supporting Information is available from the Wiley Online Library or from the author.

## Acknowledgements

The authors acknowledge the financial support from the FWO (Fund for Scientific Research-Flanders, projects I002418N and G0F9322N).

## Conflict of Interest

The authors declare no conflict of interest.

Received: ()
Revised: ()
Published online: ()

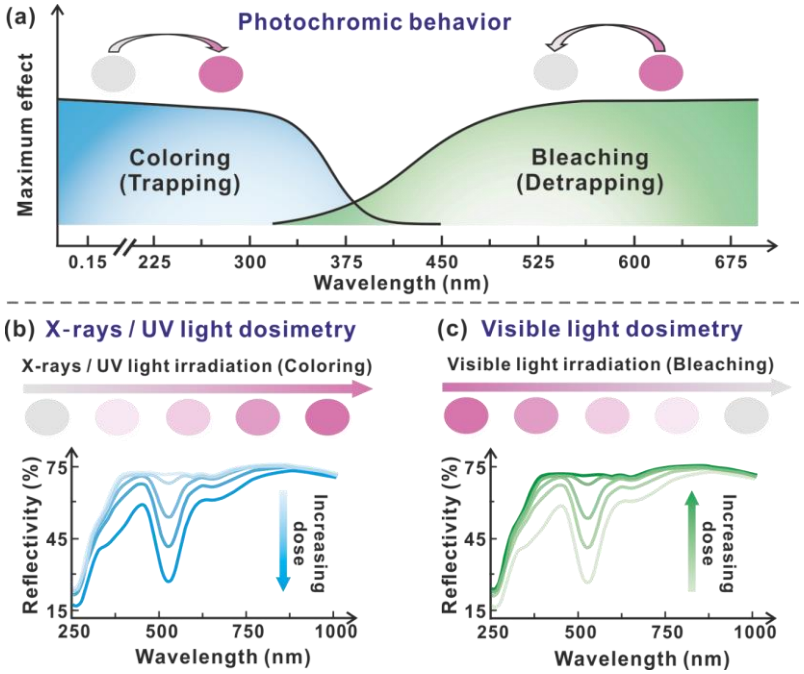


**Figure 1.** Schematic diagram showing how $BaMgSiO_4$ can be used for X-rays, UV and visible light dosimetry. a) Wavelength-dependent maximum photochromic coloring and bleaching of $BaMgSiO_4$. b) Under X-rays/UV irradiation, the white to pink coloring process can be used for X-rays/UV dosimetry. c) Under visible light irradiation, the pink to white bleaching process can be used for visible light dosimetry.

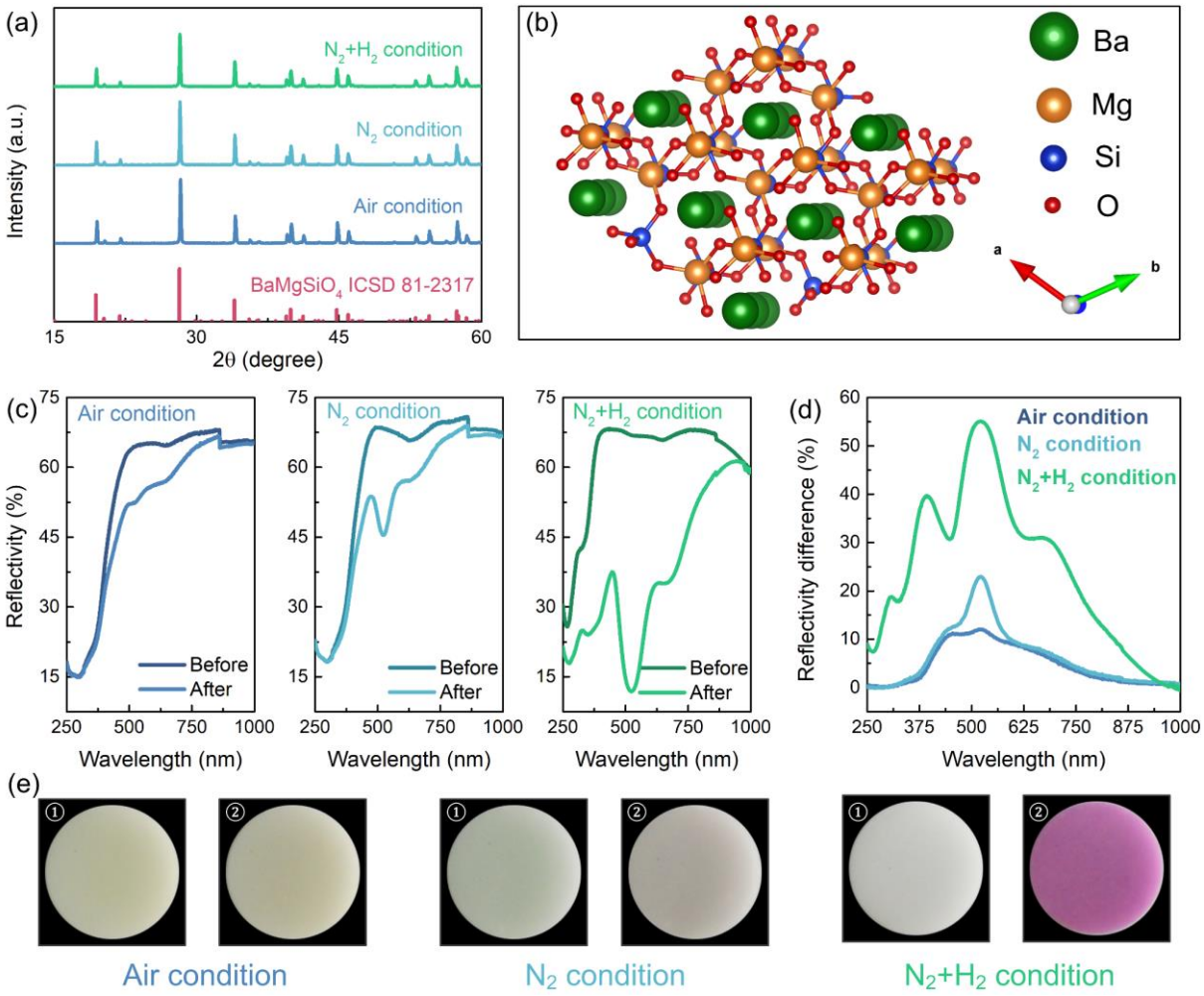


**Figure 2.** a) XRD patterns of $BaMgSiO_4$ ceramics sintered in different conditions. b) Crystal structure of $BaMgSiO_4$. c) Reflectivity and d) reflectivity difference spectra of $BaMgSiO_4$ ceramics sintered in different conditions before and after 250 nm irradiation. e) Photographs of $BaMgSiO_4$ ceramics before (①) and after 250 nm irradiation (②). Left to right: air, $N_2$ and $N_2$+$H_2$.

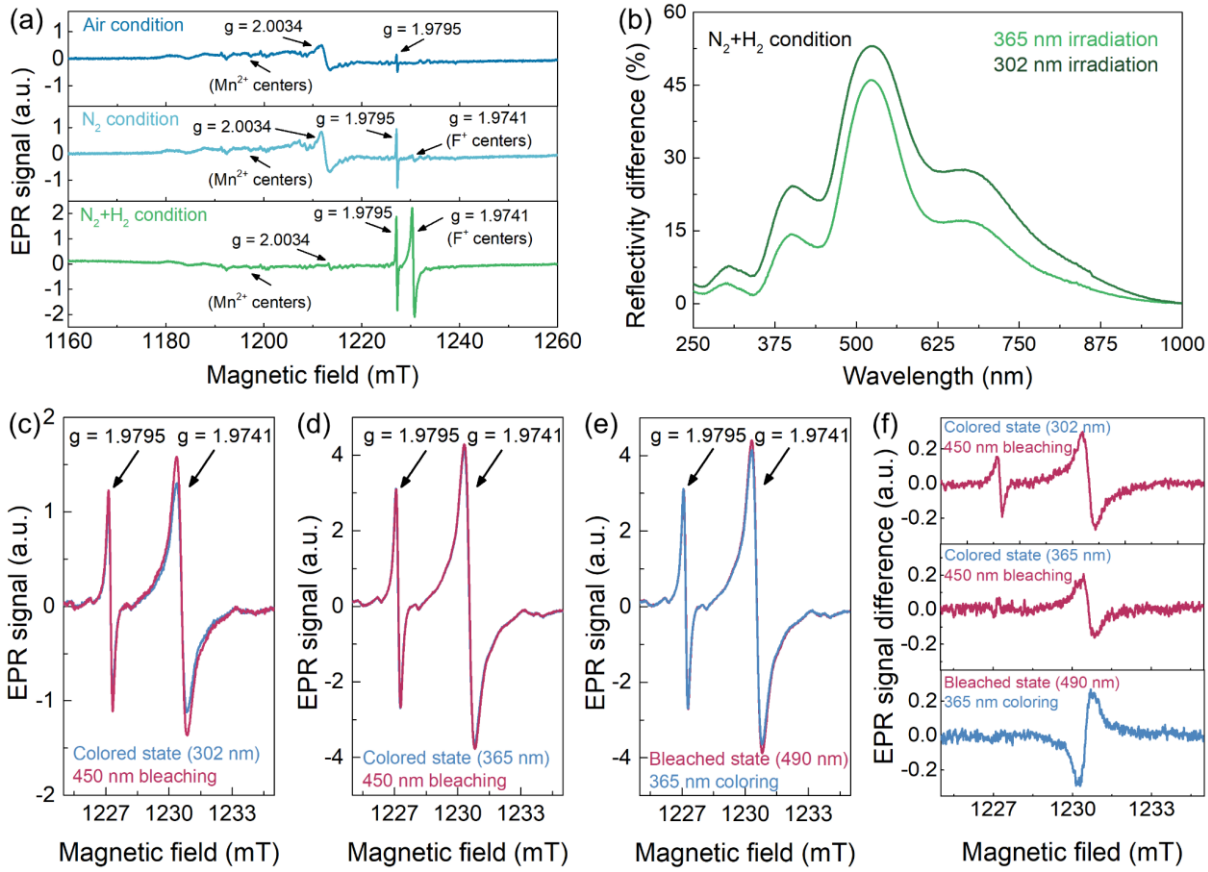


**Figure 3.** a) EPR spectra of $BaMgSiO_4$ samples sintered in air, in $N_2$ and in $N_2$+$H_2$. b) Reflectivity difference spectra of $BaMgSiO_4$ sintered in $N_2$+$H_2$ condition after irradiation at 365 nm and 302 nm. EPR spectra of $BaMgSiO_4$ samples sintered in $N_2$+$H_2$ condition for the bleaching processes c) (first 302 nm coloring and then *in situ* 450 nm bleaching), d) (first 365 nm coloring and then *in situ* 450 nm bleaching) and e) the coloring processes (first 490 nm bleaching and then *in situ* 365 nm coloring). f) EPR signal difference between the bleached and the colored $BaMgSiO_4$ samples during different irradiation processes.

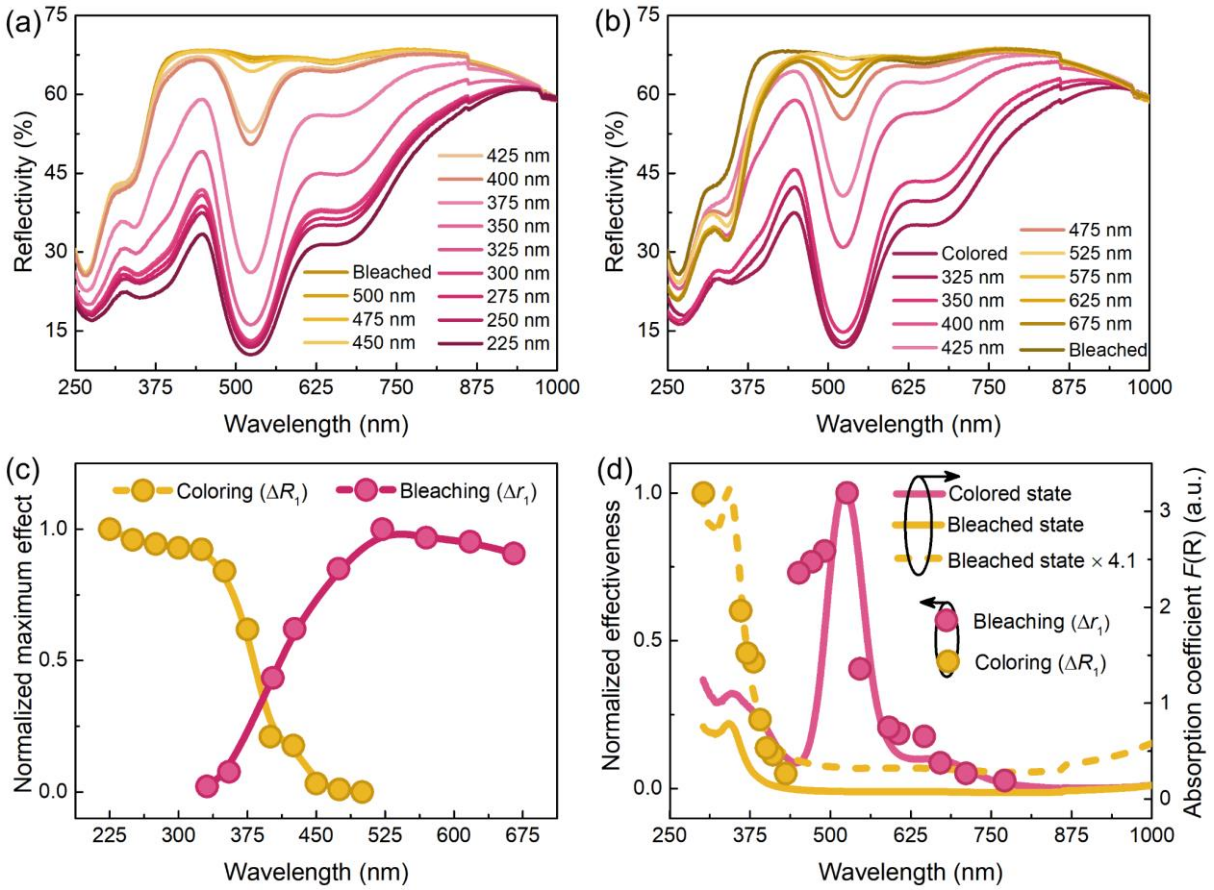


**Figure 4.** a) Reflectivity of $BaMgSiO_4$ sintered in $N_2$+$H_2$ after coloring at different wavelengths. Before irradiation at each wavelength, the sample was fully bleached by thermal treatment. b) Reflectivity of $BaMgSiO_4$ sintered in $N_2$+$H_2$ after bleaching at different wavelengths. Before irradiation at each wavelength, the sample was fully colored upon 250 nm irradiation. c) Maximum coloring or bleaching effect as a function of wavelength. d) Effectiveness of different wavelengths for coloring (yellow circles) or bleaching (pink circles) under the same power density and the same irradiation time. The yellow line represents the absorption spectrum of the sample in the bleached state and the pink line represents the absorption spectrum of the sample in the colored state. For a better comparison, the dashed yellow line represents the absorption spectrum of the sample in the bleached state multiplied by 4.1.

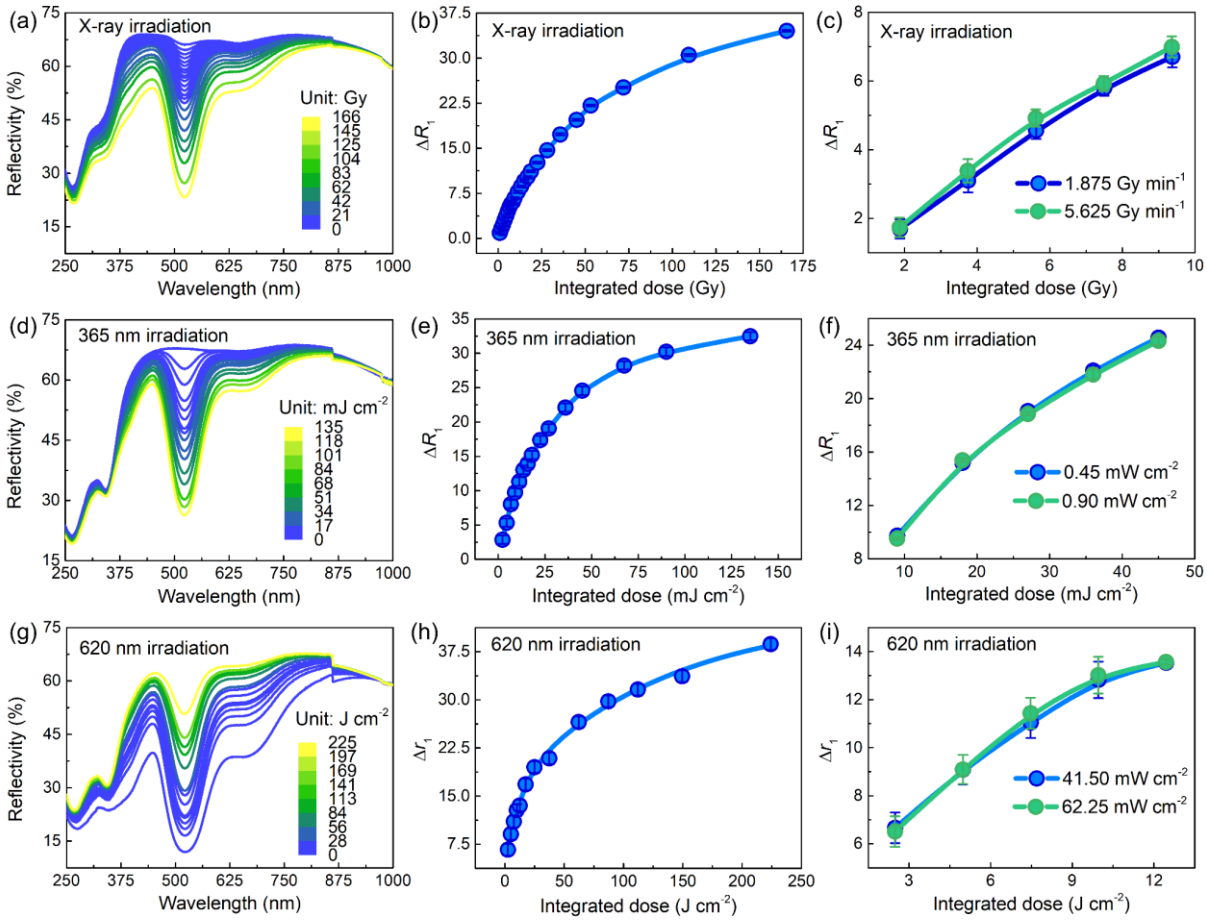


**Figure 5.** a) Reflectivity of $BaMgSiO_4$ after X-ray irradiation (1.875 Gy $min^{-1}$) for different doses. b) Dependence of $\Delta R_1$ (coloring) as a function of integrated X-ray irradiation dose. c) Dosimetry behavior of $BaMgSiO_4$ under different irradiation intensities of X-rays. d) Reflectivity of $BaMgSiO_4$ after 365 nm irradiation (0.45 mW $cm^{-2}$) for different doses. e) Dependence of $\Delta R_1$ (coloring) as a function of integrated 365 nm irradiation dose. f) Dosimetry behavior of $BaMgSiO_4$ under different irradiation intensities of 365 nm light. g) Reflectivity of $BaMgSiO_4$ after 620 nm irradiation (41.5 mW $cm^{-2}$) for different doses. h) Dependence of $\Delta r_1$ (bleaching) as a function of integrated 620 nm irradiation dose. i) Dosimetry behavior of $BaMgSiO_4$ under different irradiation intensities of 620 nm light.

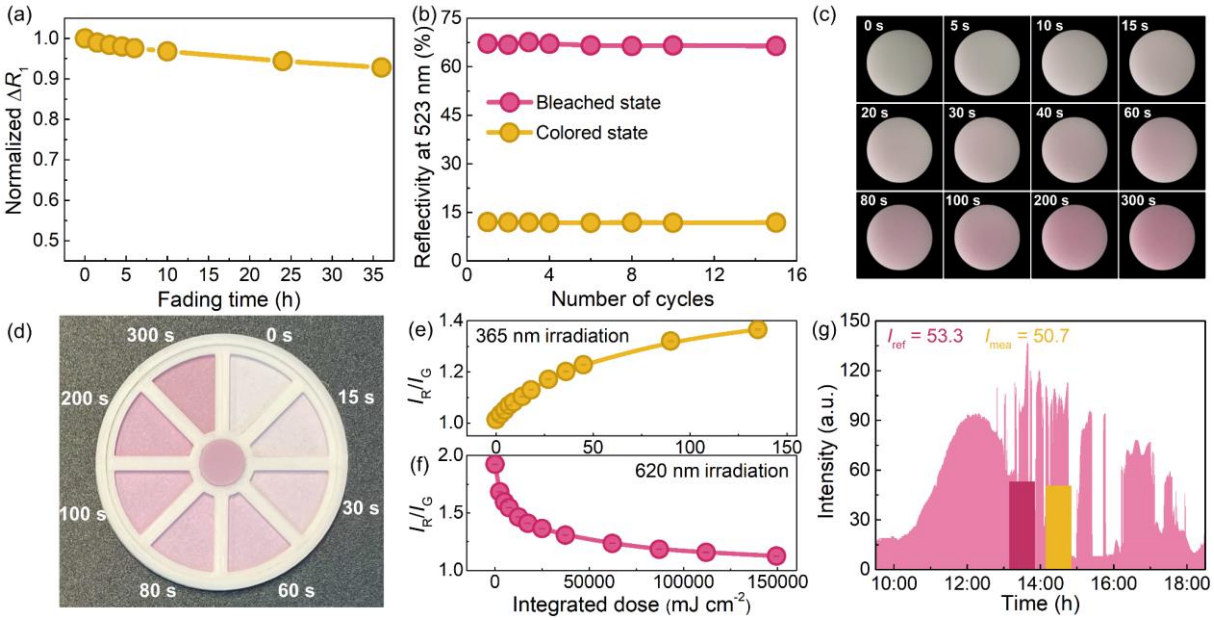


**Figure 6.** a) Fading characteristics of the photochromic behavior of $BaMgSiO_4$ sintered in $N_2$+$H_2$. b) Cycling properties of the sample upon alternating 250 nm irradiation and 285 °C thermal treatment. c) Photographs of $BaMgSiO_4$ sintered in $N_2$+$H_2$ after different times of 365 nm irradiation with a fixed power density of 0.45 mW cm$^{-2}$. The photographs were taken with a digital camera under an incandescent lamp. d) The proof-of-concept dosimeter used for colorimetric detection of irradiation dose. e) Red to green pixel intensity ($I_R/I_G$) as a function of 365 nm irradiation dose. f) Red to green pixel intensity ($I_R/I_G$) as a function of 620 nm irradiation dose. g) The demonstration of $BaMgSiO_4$-based light dosimeters for continuous daylight measurements. The red curve represents the real-time light intensity recorded using a filtered electronic lux-meter, limiting the measurement to near-UV light. The red bar and the yellow bar are the average light intensity obtained by the electronic lux-meter and the $BaMgSiO_4$-based light dosimeters, respectively.

**References**

[1] D.E. Dolmans, D. Fukumura, R.K. Jain, *Nat. Rev. Cancer.* **2003**, *3*, 375.

[2] K. Song, M. Mohseni, F. Taghipour, *Water Res.* **2016**, *94*, 341.

[3] A. Sakdinawat, D. Attwood, *Nature Photon.* **2010**, *4*, 840.

[4] R. Marin, E. Ximendes, D. Jaque, *Light: Sci. Appl.* **2022**, *11*, 65.

[5] U.V. Pedmale, S.C. Huang, M. Zander, B.J. Cole, J. Hetzel, K. Ljung, P.A.B. Reis, P. Sridevi, K. Nito, J.R. Nery, J.R. Ecker, J. Chory, *Cell* **2016**, *164*, 233.

[6] M. Lassmann, U. Eberlein, *J. Nucl. Med.* **2018**, *59*, 1494.

[7] R. Dang, B. Wang, X. Song, F. Zhang, G. Liu, *Sci. Rep.* **2021**, *11*, 10951.

[8] S. Madronlch, F.R.d. Gruiji, *Nature* **1993**, *386*, 23.

[9] S.Y. Heo, J. Kim, P. Gutruf, A. Banks, P. Wei, R. Pielak, G. Balooch, Y. Shi, H. Araki, D. Rollo, C. Gaede, M. Patel, J.W. Kwak, A.E. Peña-Alcántara, K.-T. Lee, Y. Yun, J.K. Robinson, S. Xu, J.A. Rogers, *Sci. Transl. Med.* **2018**, *10*, eaau1643.

[10] W. Zou, M. Sastry, J.J. Gooding, R. Ramanathan, V. Bansal, *Adv. Mater. Technol.* **2020**, *5*, 1901036.

[11] S. Dhanekar, K. Rangra, *Adv. Mater. Technol.* **2021**, *6*, 2000895.

[12] H. Schrader, *Metrologia* **2007**, *44*, S53.

[13] H. Wu, Y. Ge, G. Niu, J. Tang, *Matter* **2021**, *4*, 144.

[14] Q. Chen, J. Wu, X. Ou, B. Huang, J. Almutlaq, A.A. Zhumekenov, X. Guan, S. Han, L. Liang, Z. Yi, J. Li, X. Xie, Y. Wang, Y. Li, D. Fan, D.B.L. Teh, A.H. All, O.F. Mohammed, O.M. Bakr, T. Wu, M. Bettinelli, H. Yang, W. Huang, X. Liu, *Nature* **2018**, *561*, 88.

[15] Y. Zhou, J. Chen, O.M. Bakr, O.F. Mohammed, *ACS Energy Lett.* **2021**, *6*, 739.

[16] Z. Lin, S. Lv, Z. Yang, J. Qiu, S. Zhou, *Adv. Sci.* **2022**, *9*, 2102439.

[17] L. Xie, Z. Hong, J. Zan, Q. Wu, Z. Yang, X. Chen, X. Ou, X. Song, Y. He, J. Li, Q. Chen, H. Yang, *Adv. Mater.* **2021**, *33*, 2101852.

[18] H.L. Park, H. Kim, D. Lim, H. Zhou, Y.H. Kim, Y. Lee, S. Park, T.W. Lee, *Adv. Mater.* **2020**, *32*, 1906899.

[19] A. Saha, G. Kumar, S. Pradhan, G. Dash, R. Viswanathab, G. Konstantatos, *Adv. Mater.* **2022**, *34*, 2109498.

[20] W. Song, J. Chen, Z. Li, X. Fang, *Adv. Mater.* **2021**, *33*, 2101059.

[21] J. Feng, C. Gong, H. Gao, W. Wen, Y. Gong, X. Jiang, B. Zhang, Y. Wu, Y. Wu, H. Fu, L. Jiang, X. Zhang, *Nat. Electron.* **2018**, *1*, 404.

[22] H. Chen, K. Liu, L. Hu, A.A. Al-Ghamdi, X. Fang, *Mater. Today* **2015**, *18*, 493.

[23] X. Zhou, Q. Zhang, L. Gan, X. Li, H. Li, Y. Zhang, D. Golberg, T. Zhai, *Adv. Funct. Mater.* **2016**, *26*, 704.

[24] Z. Li, Z. Li, C. Zuo, X. Fang, *Adv. Mater.* **2022**, *34*, 2109083.

[25] S. Kaushik, R. Singh, *Adv. Optical Mater.* **2021**, *9*, 2002214.

[26] B. Diffey, *Atmosphere* **2020**, *11*, 125.

[27] D. Van der Heggen, R. Zilenaite, E. Ezerskyte, V. Fritz, K. Korthout, D. Vandenberghe, J. De Grave, J. Garrevoet, L. Vincze, D. Poelman, J.J. Joos, P.F. Smet, *Adv. Funct. Mater.* **2021**, *32*, 2109635.

[28] J. Wang, A.S. Jeevarathinam, A. Jhunjhunwala, H. Ren, J. Lemaster, Y. Luo, D.P. Fenning, E.E. Fullerton, J.V. Jokerst, *Adv. Mater. Technol.* **2018**, *3*, 1800037.

[29] E.G. Yukihara, S.W.S. McKeever, C.E. Andersen, A.J.J. Bos, I.K. Bailiff, E.M. Yoshimura, G.O. Sawakuchi, L. Bossin, J.B. Christensen, *Nat. Rev. Methods Primers* **2022**, *2*, 1.

[30] H. Lu, H. Hou, Y.C. Hou, Z. Zheng, Y. Ma, Z. Zhou, X. Guo, Q.J. Pan, Y. Wang, Y. Qian, J.Q. Wang, J. Lin, *J. Am. Chem. Soc.* **2022**, *144*, 3449.

[31] Z. Yang, J. Hu, D. Van der Heggen, A. Feng, H. Hu, H. Vrielinck, P.F. Smet, D. Poelman, *Adv. Funct. Mater.* **2022**, *32*, 2201684.

[32] T. Yanagida, G. Okada, N. Kawaguchi, *J. Lumin.* **2019**, *207*, 14.

[33] A. Davis, G.H.W. Deane, B.L. Diffey, *Nature* **1976**, *261*, 169.

[34] S. Cai, C. Zuo, J. Zhang, H. Liu, X. Fang, *Adv. Funct. Mater.* **2021**, *31*, 2100026.

[35] W. Kurz, A.K. Yetisen, M.V. Kaito, M.J. Fuchter, M. Jakobi, M. Elsner, A.W. Koch, *Adv. Optical Mater.* **2020**, *8*, 1901969.

[36] H. Araki, J. Kim, S. Zhang, A. Banks, K.E. Crawford, X. Sheng, P. Gutruf, Y. Shi, R.M. Pielak, J.A. Rogers, *Adv. Funct. Mater.* **2017**, *27*, 1604465.

[37] A.B.A. Kayani, S. Kuriakose, M. Monshipouri, F.A. Khalid, S. Walia, S. Sriram, M. Bhaskaran, *Small* **2021**, *17*, 2100621.

[38] H. Liu, H. Qin, N. Shen, S. Yan, Y. Wang, X. Yin, X. Chen, C. Zhang, X. Dai, R. Zhou, X. Ouyang, Z. Chai, S. Wang, *Angew Chem. Int. Ed.* **2020**, *59*, 15209.

[39] Z. Yang, J. Du, L.I.D.J. Martin, D. Van der Heggen, D. Poelman, *Laser Photonics Rev.* **2021**, *15*, 2000525.

[40] A.T. Smith, H. Ding, A. Gorski, M. Zhang, P.A. Gitman, C. Park, Z. Hao, Y. Jiang, B.L. Williams, S. Zeng, A. Kokkula, Q. Yu, G. Ding, H. Zeng, L. Sun, *Matter* **2020**, *2*, 680.

[41] M. Akiyama, *Appl. Phys. Lett.* **2010**, *97*, 181905.

[42] K. Asami, J. Ueda, S. Tanabe, *J. Lumin.* **2019**, *207*, 246.

[43] Z. Hu, X. Huang, Z. Yang, J. Qiu, Z. Song, J. Zhang, G. Dong, *Light: Sci. Appl.* **2021**, *10*, 140.

[44] J. Xie, Y. Wang, W. Liu, X. Yin, L. Chen, Y. Zou, J. Diwu, Z. Chai, T.E. Albrecht-Schmitt, G. Liu, S. Wang, *Angew. Chem. Int. Ed. Engl.* **2017**, *56*, 7500.

[45] W. Zou, A. Gonzalez, D. Jampaiah, R. Ramanathan, M. Taha, S. Walia, S. Sriram, M. Bhaskaran, J.M. Dominguez-Vera, V. Bansal, *Nat. Commun.* **2018**, *9*, 3743.

[46] H. Lu, J. Xie, X.Y. Wang, Y. Wang, Z.J. Li, K. Diefenbach, Q.J. Pan, Y. Qian, J.Q. Wang, S. Wang, J. Lin, *Nat. Commun.* **2021**, *12*, 2798.

[47] T. Lyu, P. Dorenbos, C. Li, Z. Wei, *Laser Photonics Rev.* **2022**, *16*, 2200055.

[48] Z. Wang, Y. Wang, Z. Ge, Y. Tian, M. Ai, S. Cao, M. Wang, S. Wang, J. Ma, *Matter* **2022**,

[49] W. Liu, X. Dai, J. Xie, M.A. Silver, D. Zhang, Y. Wang, Y. Cai, J. Diwu, J. Wang, R. Zhou, Z. Chai, S. Wang, *ACS Appl. Mater. Interfaces* **2018**, *10*, 4844.

[50] P.S. Khiabani, A.H. Soeriyadi, P.J. Reece, J.J. Gooding, *ACS Sens.* **2016**, *1*, 775.

[51] A.S. Finny, C. Jiang, S. Andreescu, *ACS Appl. Mater. Interfaces* **2020**, *12*, 43911.

[52] K. Pushpavanam, S. Inamdar, S. Dutta, T. Bista, T. Sokolowski, E. Boshoven, S. Sapareto, K. Rege, *Sci. Adv.* **2019**, *5*, eaaw8704.

[53] K. Pushpavanam, S. Inamdar, J. Chang, T. Bista, S. Sapareto, K. Rege, *Adv. Funct. Mater.* **2017**, *27*, 1606724.

[54] A.J. Venning, K.N. Nitschke, P.J. Keall, C. Baldock, *Med. Phys.* **2005**, *32*, 1047.

[55] M. Jaszczak, E. Sasiadek-Andrzejczak, M. Kozicki, *Materials* **2022**, *15*, 2546.

[56] J.L. Butterfield, S.P. Keyser, K.V. Dikshit, H. Kwon, M.I. Koster, C.J. Bruns, *ACS Nano* **2020**, *14*, 13619.

[57] I. Norrbo, A. Curutchet, A. Kuusisto, J. Mäkelä, P. Laukkanen, P. Paturi, T. Laihinen, J. Sinkkonen, E. Wetterskog, F. Mamedov, T. Le Bahers, M. Lastusaari, *Mater. Horiz.* **2018**, *5*, 569.

[58] D.J. Wilson, F.J. Martin-Martinez, L.F. Deravi, *ACS Sens.* **2022**, *7*, 523.

[59] Z. Zheng, H. Lu, X. Guo, Z. Zhou, Y. Wang, Z.J. Li, G.P. Xiao, Y. Qian, J. Lin, J.Q. Wang, *Chem. Commun.* **2021**, *57*, 8131.

[60] H. Zhang, X. Wu, *Adv. Sci.* **2016**, *3*, 1500224.

[61] J. Zhao, L. Liu, Y. Zhang, Z. Feng, F. Zhao, W. Wang, *Nano Res.* **2020**, *14*, 165.

[62] J. Xie, Y. Wang, W. Liu, C. Liang, Y. Zhang, L. Chen, D. Sheng, Z. Chai, S. Wang, *Sci. China Chem.* **2020**, *63*, 1608.

[63] J. Xie, Y. Wang, D. Zhang, C. Liang, W. Liu, Y. Chong, X. Yin, Y. Zhang, D. Gui, L. Chen, W. Tong, Z. Liu, J. Diwu, Z. Chai, S. Wang, *Chem. Commun.* **2019**, *55*, 11715.

[64] L. Jiang, W. Li, J. Nie, R. Wang, X. Chen, W. Fan, L. Hu, *ACS Sens.* **2021**, *6*, 1643.

[65] T. He, J. Yao, *Prog. Mater. Sci.* **2006**, *51*, 810.

[66] G.R. Ferreira, A.M. Tannure, L.C. Cardoso, M.F. Siqueira, A.G.C. Bianchi, R.F. Bianchi, *Sensor. Actuat. B-Chem.* **2017**, *240*, 1003.

[67] Y. Zhu, H.Q. Sun, Q.N. Jia, L.L. Guan, D.F. Peng, Q.W. Zhang, X.H. Hao, *Adv. Optical Mater.* **2021**, *9*, 2001626.

[68] Y. Ren, Z. Yang, Y. Wang, M. Li, J. Qiu, Z. Song, J. Yu, A. Ullah, I. Khan, *Sci. China Mater.* **2020**, *63*, 582.

[69] Z. Yang, J. Du, L.I.D.J. Martin, A. Feng, E. Cosaert, B. Zhao, W. Liu, R. Van Deun, H. Vrielinck, D. Poelman, *Adv. Optical Mater.* **2021**, *9*, 2100669.

[70] B. Liu, J. Barbier, *J. Solid State Chem.* **1993**, *102*, 115.

[71] W. Ji, M.H. Lee, L. Hao, X. Xu, S. Agathopoulos, D. Zheng, C. Fang, *Inorg. Chem.* **2015**, *54*, 1556.

[72] W.B. Dai, K. Huang, Y.M. Fan, H. Li, M. Xu, *J. Lumin.* **2020**, *222*, 117137.

[73] L.E. Halliburton, N.C. Giles, N.Y. Garces, M. Luo, C. Xu, L. Bai, L.A. Boatner, *Appl. Phys. Lett.* **2005**, *87*, 172108.

[74] X. Wu, J. Lin, Z. Xu, C. Zhao, C. Lin, H. Wang, T. Lin, X. Zheng, B. Sa, Q. Zhang, K. Wang, Z. Sun, J. Zhai, *Laser Photonics Rev.* **2021**, *15*, 2100211.

[75] M. Tsuta, S. Nakamura, A. Kato, *Opt. Laser Technol.* **2021**, *135*, 106725.

[76] D. Van der Heggen, J.J. Joos, P.F. Smet, *ACS Photonics* **2018**, *5*, 4529.

[77] Z. Yang, J. Hu, L.I.D.J. Martin, D. Van der Heggen, D. Poelman, *J. Mater. Chem. C* **2021**, *9*, 14012.

[78] P. Kubelka, F. Munk, *Z. Technol. Phys.* **1931**, *12*, 593.

**Keywords:** passive dosimeter, $BaMgSiO_4$, photochromic materials, cumulative dose, coloring and bleaching, oxygen vacancies

Z. Yang, J. Hu, D. Van der Heggen*, M. Jiao, A. Feng, H. Vrielinck*, P. F. Smet and D. Poelman*

**A Versatile Photochromic Dosimeter enabling Detection of X-ray, Ultraviolet, and Visible Photons**

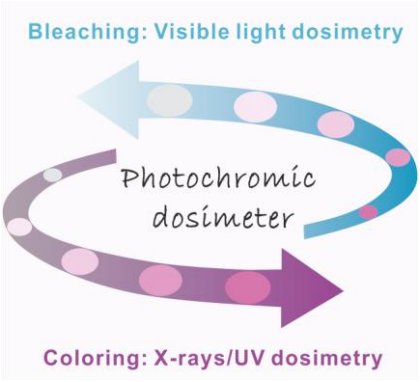


An all-round dosimeter for X-ray, ultraviolet, and visible photons detection is reported based on photochromic material $BaMgSiO_4$. Electron paramagnetic resonance measurements and irradiation wavelength- and power-dependent experiments are systematically carried out to provide a deeper insight into the photochromic behavior. In combination with the advantages of power-free, convenient readout processes and excellent stability, $BaMgSiO_4$ can be an ideal integrating dosimeter.